RESEARCH ARTICLE

Micro-mechanical analysis on the onset of erosion in granular materials

H.M.D.Harshani[a*] S.A.Galindo-Torres[a] A.Scheuermann[a] and H.B. Muhlhaus[b]

[a]*School of Civil Engineering, The University of Queensland, Australia,*

[b]*School of Earth Sciences, The University of Queensland, Australia,*
(*Received 00 Month 200x; final version received 00 Month 200x*)

The onset of internal erosion is a particle level phenomenon, and therefore, a numerical model capable of tracking the behaviour of particles at micro-scale is needed to exemplify most of the critical variables involved in the process. In this paper, a three dimensional fully coupled fluid-solid model was utilized to explore the initiation of erosion. Particles were modelled on a micro-scale using the Discrete Element Method (DEM) while the fluid was modelled at a meso-scale using the Lattice Boltzmann Method (LBM). Fluid was passed through a solid matrix in an opposing direction to gravity with the pore water pressure controlled in step-wise stages until internal erosion or bulk movement of the particles developed and progressed. The model was validated through experimental results found in the literature. Once validated, particle fluid properties were analyzed for the onset of erosion. Determination of a critical hydraulic gradient was obtained from the modelled scenario, which gave clear evidence that the coupled DEM-LBM scheme is a very effective tool for studying internal erosion phenomena in water retaining structures.

Keywords: Piping erosion, Lattice Boltzmann Method (LBM), Discrete Element Method (DEM), critical hydraulic gradient

1. Introduction

Internal erosion is the loosening, detachment and transport of fine particles through the pore structure of a coarse material due to seepage flow. The ongoing erosion and transport of particles along a flow path may lead to initiation and progressive development of internal deformation of the particle structure leading to critical situations for the stability of the overall construction. This phenomenon occurs mainly within water retaining structures such as embankment dams, levees and dikes built with geo-materials [1], but it can also take place in the foundation of structures that are, frequently composed of alluvial soils. Dysfunctions of these water retaining structures due to internal erosion processes have been reported to account for the failure of approximately half of the embankment dams and levees throughout the world [3]. **These internal erosion mechanisms appear in several forms, including piping, concentrated leak erosion, contact erosion and suffusion [2].**

The onset of any kind of erosion process is dependent on the hydraulic, mechanical and geometrical conditions on the particle scale. The mechanisms involved in
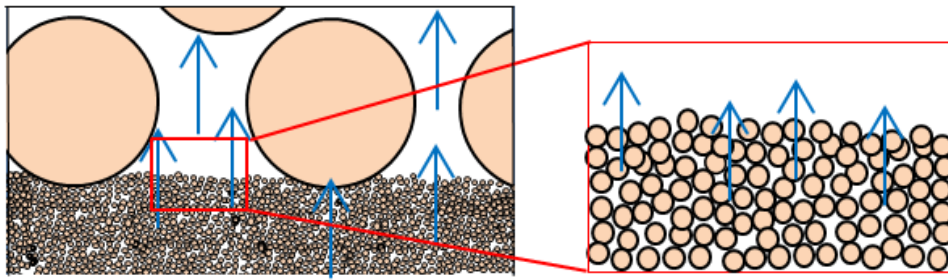
Taylor & Francis and I.T. Consultant

Figure 1. Initiation of contact erosion mechanism at micro-scale.

the process of erosion include mechanical interaction between grains, hydrodynamic changes of fluid along the channels formed by the interconnected pore space and hydro-mechanical interaction at the solid-fluid boundary. The initiation of translational and rotational movement of solid particles due to these processes can be studied only through models **representing and allowing the observation of processes and changes of properties on the particle scale. Physical experiments can be conducted on the particle scale using solids and fluid, which are refractive index matched, combined with Particle Imaging Velocimetry to determine the flow field in the pores formed by the solid grains [4]. However, in these kinds of tests certain micro-scale material properties or reactions are not assessable or observable. To fill this gap, micro-scale numerical models can be used not only to track movement and forces applied on individual particles, but also to quantitatively study the interaction between driving fluid flow and particle reaction** during the erosion process.

The Discrete Element Method (DEM) is one of the numerical tools which **can be** used to model the behaviour of granular materials. DEM was first proposed by Cundall **and Strack** in the 1970s [5]. It is based on the description of the material behaviour as a collection of individual particles interacting at contact points. Although the computational cost **of** DEM **is significant**, it has already been applied **to many** geotechnical engineering problems [5–8]. The challenging task **for the considered problem of erosion** is to extend DEM for problems covering the interaction of the fluid with the solid particles [9]. Several methods have been developed and presented in literature to account for the interaction between fluid and solids on **the** macro scale. **However,** the local discontinuous nature of the material **is usually not considered** [10–12]. EI Shamy and Zegal [13] developed a coupled continuum discrete model for saturated granular soil which idealized the fluid motion using an averaged Navier-Stokes equation. Simulation results have shown the complex response patterns during the onset of quicksand conditions and have provided valuable information about the associated mechanisms. In **their** method the fluid equations of motion are solved by **a** standard Computational Fluid Dynamics (CFD) model which is based on the Eulerian formulation. **Fluidisation of** soil and piping were simulated using the coupled flow method of Xiao and Yuan [14]. **The numerical results of this model were found to be consistent with published experimental results. However, the coupling of conventional CFD models with discrete methods, such as the DEM, can be challenging in terms of realistically applying the drag and bouyancy forces from the CFD on the DEM particles.**

The **Lattice Boltzmann Method** (LBM) has recently become **an alternative approach for simulating fluid flow on a pore scale, since it provides a force distribution over the particles in a reasonably high resolution and**

has the capability of dealing with complex geometries. Fluid is modelled by **a probabilistic density of** particles that move on a regular lattice to adjacent points and then **re-distribute** their momentum in subsequent collisions. The hydrodynamic interaction of the fluid with the solid phase is introduced through the coupling of LBM and DEM. It has been shown that the coupling reproduces both the drag and bouyancy forces due to the fluid [15]. Derksen [16], Lomine et al. [17] and Abdelhamid and **EI Shamy** [18] simulated particle erosion by using LBM coupled with DEM. **The initiation and development of the internal erosion process also has been analyzed using continuum models at the macro scale [19]. However, it is extremely difficult to introduce processes occurring at the micro-scale in these models.**

In the present study, a DEM/LBM method of Galindo-Torres **et al.** [15] is used for **investigating** hydraulically induced contact erosion with the focus on identifying changes in the assembly of particles **subject to erosion** showing the start or onset of the erosion process. **For this purpose, the study focusses on the processes taking place in the voids formed by the coarse fraction sitting on top of a layer of the fine-grained soil (Figure 1). In order to exclude mechanical influence from coarse particles and to create a computationally effective model, the study concentrates on an assembly of fine particles at the interface from fine to coarse layers. This simplification introduces an assumption, which needs to be mentioned, namely that the movement of fine particles is geometrically unhindered by the presence of coarse particles.** The content of this paper is organized as follows. In Section 2 the principles of the LBM and DEM methods are described. In the third section the developed model is introduced, and its validation is presented in section 4. Results and discussion of the present work are described in Section 5. Conclusions and future research directions are summarized in the last section.

2. Method

2.1. *Discrete Element Method*

The DEM has been extensively used to study soil and rock mechanics [15] [20]. In DEM models, particles are idealized using discrete spheres, ellipsoids or other three dimensional shapes. Although most researchers use spherical particles to reduce the complexity of contact detection, more complex shaped elements such as polygons or spheropolyhedra [21] have also been **used** [22].

In this study, spherical particles are used to model the packing of the solid phase, and forces acting on a particle in the system consist of forces arising at the contacts with neighbouring particles ($\mathbf{f_{c,ij}}$), gravitational force ($m_i\mathbf{g}$) and forces exerted by the fluid flow ($\mathbf{f_{pf,i}}$). The governing equation for a particle, i, with radius, R_i, mass, m_i, which has translational and rotational motion can be written as,

$$m_i\frac{d\mathbf{v_i}}{dt} = \mathbf{f}_{pf,i} + \sum_{j=1}^{k_c}(\mathbf{f}_{c,ij}) + m_i\mathbf{g} \tag{1}$$

$$I_i\frac{d\mathbf{w_i}}{dt} = \sum_{j=1}^{k_c}(\mathbf{T}_{t,ij} + \mathbf{T}_{r,ij}) \tag{2}$$

where $\mathbf{v_i}$ and $\mathbf{w_i}$ are translational and angular velocities, respectively, I_i is the moment of inertia, and k_c is the number of particles interacting with the particle. The torque acting on particle i by particle j **consists of** two components: $\mathbf{T_{t,ij}}$, generated by the tangential force, and $\mathbf{T_{r,ij}}$, commonly known as the rolling friction torque. In the first stage of the algorithm, inter-particle **contact** forces $(f_{c,ij})$ **can be decomposed into a** normal force F_n and **a** tangential force $\mathbf{F}_t$, which are calculated by contact laws that are a direct function of grain stiffness properties and relative movements at the contacts.

$$\mathbf{F}_n = K_n \delta_n \hat{\mathbf{n}} \tag{3}$$

where δ_n **is the overlapping length,** K_n (Figure 2(a)) is the normal stiffness of the material and $\overrightarrow{n}$ is the **unit vector** normal to the contact plane.

Particles are allowed to rotate, and hence at the contact point, $\mathbf{x}_c$, (which is defined as the middle point of the overlapping length), both particles have a relative velocity that represents the relative displacement of the particle at that point. This relative velocity ($\mathbf{v}_{rel}$) is given by,

$$\mathbf{v}_{rel} = \Omega_1 \times (\mathbf{x}_c - \mathbf{x}_1) + \mathbf{v}_1 - \Omega_2 \times (\mathbf{x}_c - \mathbf{x}_2) - \mathbf{v}_2 \tag{4}$$

where Ω_i, $\mathbf{v}_i$ and $\mathbf{x}_i$ are the angular velocity, velocity and centre of the i-th particle, respectively. This relative velocity can be decomposed into normal $\mathbf{v}_n$ and tangential $\mathbf{v}_t$ components. The tangential component given by Equation 6 is numerically integrated to obtain the tangential displacement δ_t [23] and this displacement is used to calculate the tangential force $\mathbf{F}_t$,

$$\mathbf{F}_t = K_t \delta_t \hat{\mathbf{t}} \tag{5}$$

$$\mathbf{v}_t = \mathbf{v}_{rel} - (\mathbf{v}_{rel}.\hat{\mathbf{n}})\hat{\mathbf{n}} \tag{6}$$

where $\hat{t} = \mathbf{v}_t/v_t$ and K_t is a tangential stiffness. This elastic tangential force represents the effect of static friction in the absence of roughness of the spherical particles. To be physically correct, the tangential force must be bounded by the Coulomb limit [24], and so the correct tangential force is

$$\mathbf{F}_t = \min(K_t \delta_t, \mu F_n)\hat{\mathbf{t}} \tag{7}$$

which depends on the microscopic friction coefficient μ.

For every time step of the computation, interaction forces between particles and the resulting forces acting on them, are deduced from the spheres' position through the interaction laws. At the second stage, Newtons second law is integrated to compute the new positions **and orientations** of spheres. Contact between two particles is shown in Figure 2(b) and the deformation corresponds to an overlap, δ. The particles are in collision when the distance between particles, r_{ij}, is less than the sum of the radii of two particles in contact $(R_i + R_j)$.

2.2.   *Lattice Boltzmann Method*

The LBM originated as an extension of the Lattice Gas Automata (LGA) [25]. Unlike the traditional macro level Navier-Stokes equation where fluid is treated as a
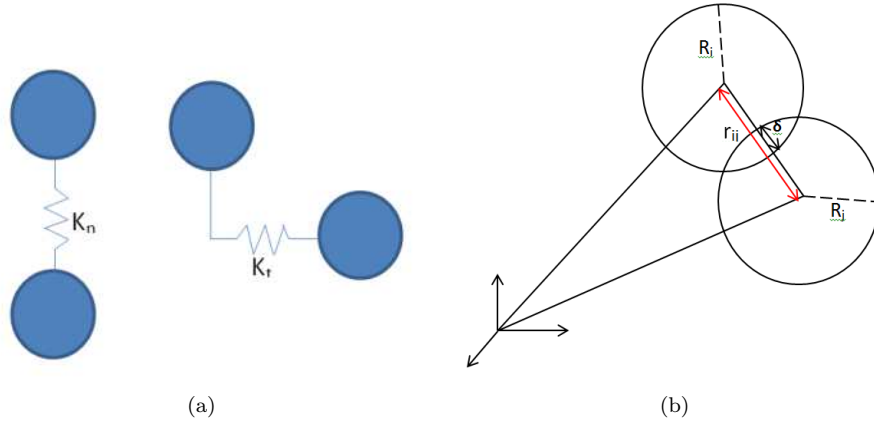
Figure 2. (a) Spring model for DEM particles. (b) Collision of two DEM particles with δ overlapping.

continuum, the LBM regards fluid as particles which perform consecutive streaming and collision processes over a discrete lattice [26]. **A lattice is characterized by the notation DnQm in which 'n' indicates the dimensions of the lattice, and 'm' represents the number of directions streaming from a lattice point along which particles can move.** In the present work three dimensional flow is modelled using the D3Q15 scheme. During a particular time step, fluid mass can propagate from a node with position x to **any of 15 directions** as shown in Figure 3(a). Possible fluid velocities at each node are represented by vector e_i and there are i=15 possible fluid velocities at each node. The macroscopic density, ρ, at each cell position, **x**, can be determined by:

$$\rho(\mathbf{x}) = \Sigma_{i=0}^{15} f_i(\mathbf{x}) \tag{8}$$

Probability distribution function, f_i, represents the density of fluid particles going through one of the 15 discrete velocities, e_i. Similarly, macroscopic velocity, **u**, at each cell position, **x**, is given by:

$$\mathbf{u}(\mathbf{x}) = \frac{\Sigma_{i=0}^{15} f_i(\mathbf{x})\mathbf{e_i}}{\rho(x)} \tag{9}$$

The LBM solves the Lattice Boltzmann equation which is discretized in both the **space** and velocity domains,

$$f_i(\mathbf{x} + \mathbf{e}_i \delta t, t + \delta t) = f_i(\mathbf{x}, t) + \Omega_{col} \tag{10}$$

where Ω_{col} is a collision operator representing the relaxation process due to collision of the fluid particles. The choice of Ω_{col} may vary for different applications. For the sake of simplicity, **the widely accepted Bhatnagar-Gross-Krook** (BGK) operator, which features a single relaxation time τ, is used for this study [27].

$$\Omega_{col} = \frac{\delta t}{\tau}(f_i^{eq} - f_i) \tag{11}$$

where f_i^{eq} is the local equilibrium distribution function. **It has been shown that Navier-Stokes equations for fluid flow [28] are recovered if f_i^{eq} has the**
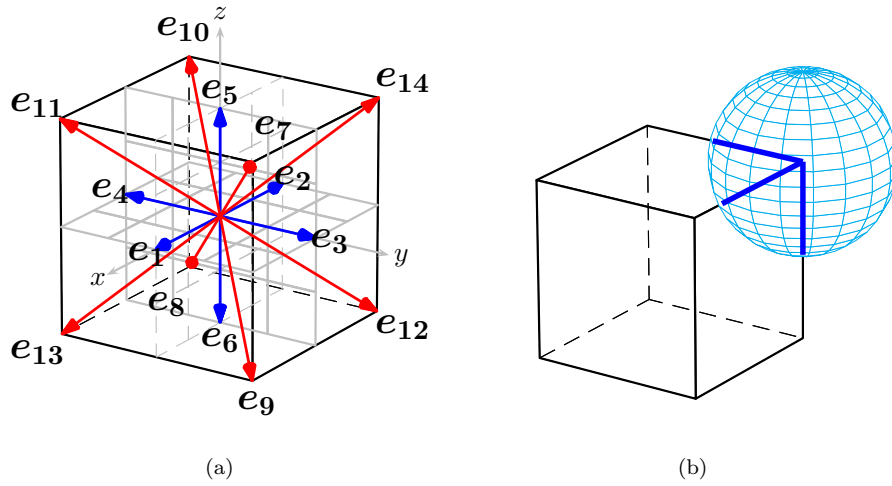
Taylor & Francis and I.T. Consultant

Figure 3.   (a) LBM cell of the D3Q15 showing the direction of each one of the 15 discrete
velocities. (b) DEM sphere interacting with an LBM cell (Galindo-Torres et al. [15]).

form,

$$f_i^{eq} = \omega_i \rho (1 + 3\frac{\mathbf{e}_i.\mathbf{u}}{C^2} + \frac{9(\mathbf{e}_i.\mathbf{u})^2}{2C^4} - \frac{3u^2}{2C^2})$$ (12)

The kinematic viscosity coefficient of the fluid, ν, can be determined as follows:

$$\nu = (\tau - 0.5)\frac{\delta_x^2}{3\delta_t}$$ (13)

In Equation 12, C refers to the lattice speed, which is defined as the ratio of the lattice space, δ_x, to the LBM time step, δ_{tlbm},

$$C = \frac{\delta_x}{\delta_t}$$ (14)

Changes in pressure, p, and density, ρ, are related by the equation of state;

$$p = \frac{C^2}{3}\rho$$ (15)

The parameter C is tuned in order to reach the incompressibility state of the fluid to ensure minimum density fluctuations across the fluid.

2.3.   *Coupled LBM and DEM*

For describing the interaction between two different phases (solid and fluid), the coupling method implemented by Galindo-Torres **et al.** [15] and Owen et al. [29] is applied for spherical particles. In LBM the fluid phase is divided into a regular lattice structure intersected by moving DEM spheres as shown in Figure 3(b). During the coupling mechanism, **Equation** 10 is modified, **as follows,** to account for the volume fraction, ε, occupied by the DEM sphere.

$$f_i(x + e_i\delta t, t + \delta t) = f_i(x,t) + (1 - B_n)\left(\frac{\delta t}{\tau}\left(f_i^{eq} - f_i\right)\right) + B_n\Omega_i^s$$ (16)
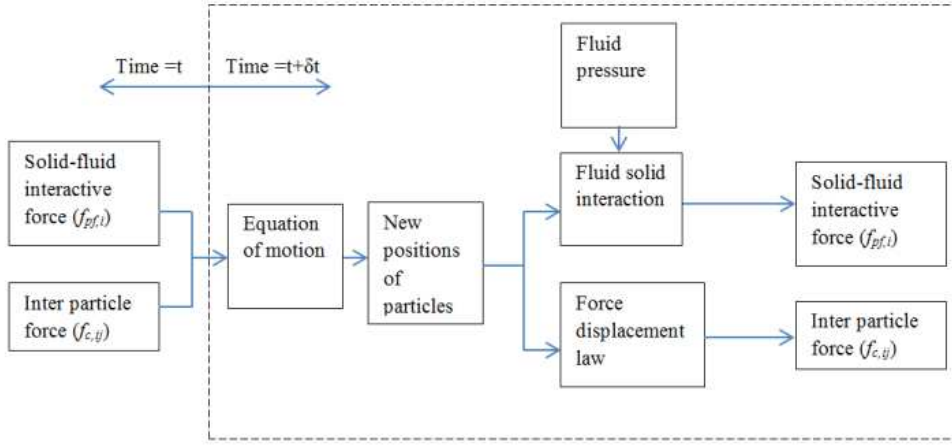
Figure 4. Algorithm for hydro mechanical model employed.

where Ω_i^s is a collision operator representing the change of momentum due to the collision of the DEM sphere within the LBM cell and B_n is a weight coverage function [29] of the form,

$$B_n(\varepsilon) = \frac{\varepsilon_n(\tau/\Delta t - 1/2)}{(1 - \varepsilon_n) + (\tau/\Delta t - 1/2)} \qquad (17)$$

Although there are various methods to calculate the volume fraction, ε, of the DEM sphere outside the edges of the LBM cell, Galindo-Torres **et al.** [15] proposed a simple approach to calculate the volume fraction by considering the intersection length. The intersection length, l_e, is computed for each of the 12 edges of the LBM cell (see Fig. 3(b)). It is then compared with the total edge length to obtain the volume fraction,

$$\varepsilon = \frac{\sum_{e=1}^{12} l_e}{12\delta_x} \qquad (18)$$

More details regarding the coupled mechanism can be found in [15].

The total force, F, exerted on the DEM sphere is computed by superimposing the change of momentum given by each of the cells that the sphere covers,

$$\mathbf{F} = \frac{\delta_x^3}{\delta_t} \sum_n B_n \left(\sum_i \Omega_i^s \mathbf{e_i} \right) \qquad (19)$$

And consequently the torque, T, is,

$$\mathbf{T} = \frac{\delta_x^3}{\delta_t} \sum_n \left[(\mathbf{x_n} - \mathbf{x_{CM}}) \times \mathbf{B_n} \left(\sum_i \mathbf{\Omega_i^s e_i} \right) \right] \qquad (20)$$

Figure 4 shows the algorithm flow chart for the coupling of solid and fluid phases.

2.4.   *Verification of the DEM/LBM model*

To validate the **DEM/LBM model**, the drag coefficient, C_D, of a sphere **immersed** in a fluid is **determined** as a function of its Reynolds number, Re,
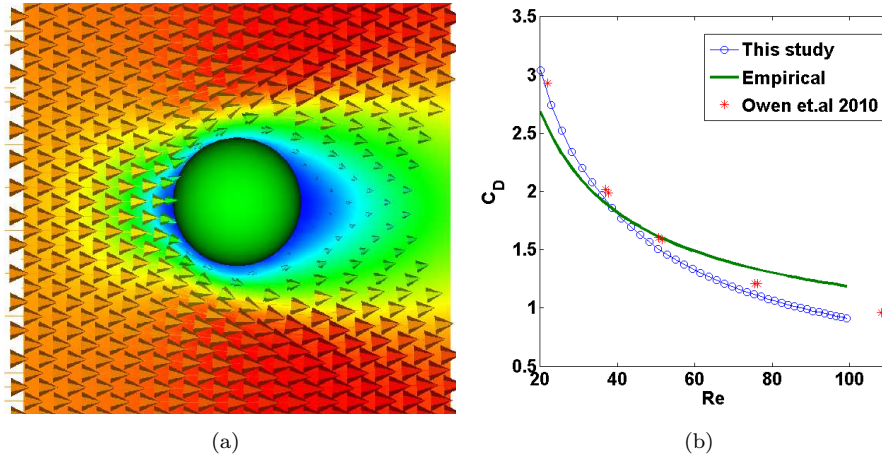
Figure 5. (a) Cross sectional contour plot of the fluid velocity field surrounding a DEM sphere for $Re = 30$ (b) Sphere drag coefficient C_D as a function of the Reynolds number, Re ([from Galindo-Torres] [22]).

and compared with the **results derived** by Owen et al. [29]. **For this purpose,** a DEM sphere with a radius of 0.036m is placed inside the LBM lattice of $240 \times 60 \times 60$ cells. The lattice space is **chosen as** $\delta_x = 0.004$m and the lattice time step $\delta_t = 1.6 \times 10^{-2}$s . The fluid density and viscosity are taken as $\rho = 1000$kg/m^3 and ν is 10^{-4}m^2/s, respectively. The velocity field surrounding the DEM sphere for a Reynolds number of 30 is shown in Figure 5(a).

The Reynolds number is calculated using the following equation:

$$Re = \frac{v_{ave}D}{\nu} \tag{21}$$

where D is the sphere's diameter and v_{ave} is the average velocities of **fluid filled** cells **of the lattice**. The drag coefficient, C_D, is calculated by the following equation:

$$C_D = \frac{2F_x}{\rho v_{ave}^2 \pi D^2/4} \tag{22}$$

where F_x is the x component of the reaction force. Figure 5(b) shows the calculated drag coefficient as a function of Re **in** comparison **to results** of a previous study by Owen et al. [29]. Additionally, an empirical correlation [31] with experimental data is also presented:

$$C_D \approx \frac{24}{Re} + \frac{6}{1 + \sqrt{Re}} + 0.4 \tag{23}$$

Although this example measured the drag force produced by fluid movement, the model also considered the buoyancy forces as shown by Galindo-Torres et al. [15]. Therefore, the coupling mechanism includes both the buoyancy of a pressure gradient over the fluid and the drag due to the fluid velocity, and as will be shown, both effects play a role in the onset of erosion.
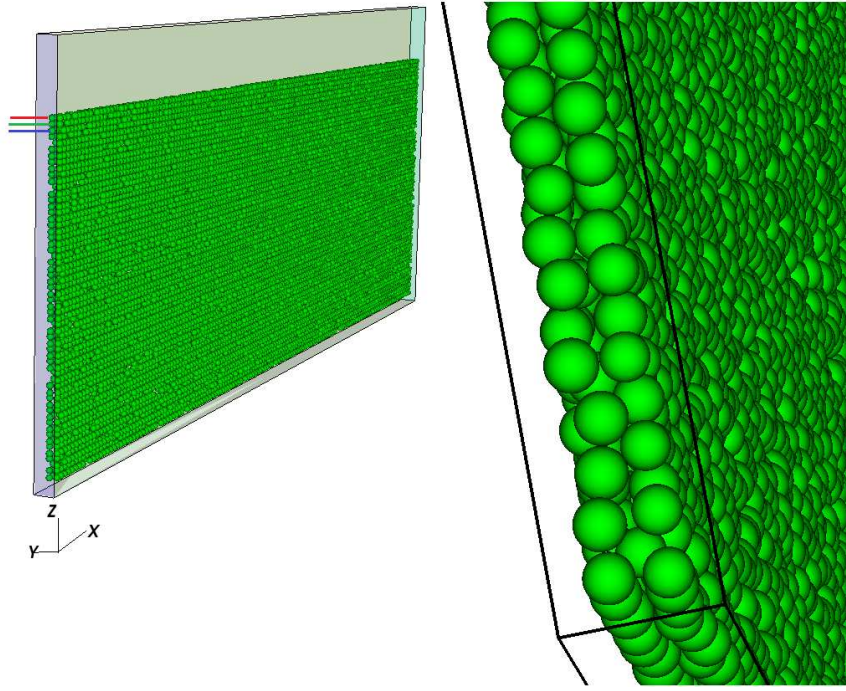
Figure 6.   DEM hexagonal packing arrangement of the granular particles inside the chamber with dimensions of X=30cm, Y=0.6cm, Z=14cm. The first three layers are highlighted for future analysis.

3.   Numerical Model

Spherical particles **of diameter 2 mm** were used to generate the granular soil packing in a rectangular chamber with rigid walls (300 mm length, 6 mm width and 140 mm in height). The particles were packed by dropping them under gravity and allowing them to settle for a sufficient time. **Ten percent of particles were then deleted randomly to introduce some disorder in the packing.** In total 31,473 particles of uniform size **were placed in the chamber as described to form granular packing covering the area of the chamber to a height of 100 mm** (Figure 6). **Then gravity was applied to force settling of the particles. The final height of the packing was 96 mm.** Table 1 shows the parameters for the DEM and the LBM models used for this study.

The space **between the container walls was** then spatially discretised with a square lattice of constant spacing, $\delta_x = 0.4$ mm, by dividing the container into 750*15*350 cells. **Consequently, the lattice was 44 mm higher than the granular packing to avoid the movement of particles out of the volume when fluid motion was calculated.** A coarser lattice grid would have resulted in an insufficient resolution for describing the micro-scale effect. Unfortunately, due to the large memory requirement and computational time **for calculating this model**, it was not possible to **use** a finer grid arrangement.

Figure 7(a) shows the DEM sample **within** the LBM domain. The LBM fluid density is **given a value of** 1,000 kg/m^3. Gravity is applied only to the particles **in the DEM simulation**. The pressure gradient across the sample was increased by maintaining a constant pressure at the top of the wall **at 140 mm height**, while the pressure at the base was raised incrementally until clear translation**al** movement of particles could be seen (Figure 7(b)). **The applied pressure gradient introduces fluid flow in an upward direction.** As described in Section 2, this pressure variation is applied by changing the density between top and bot-
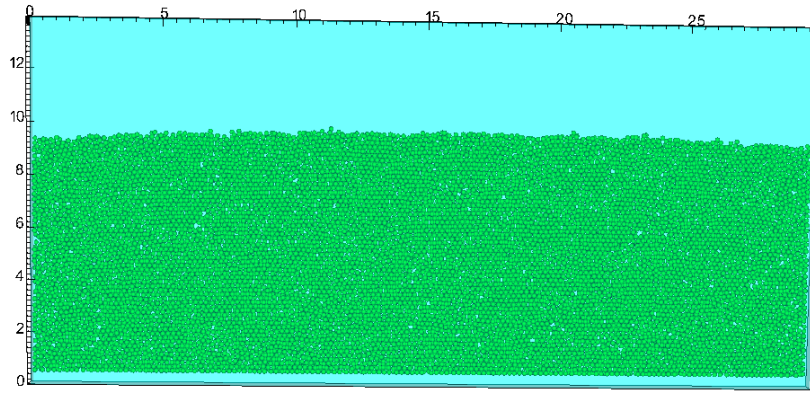
(a)
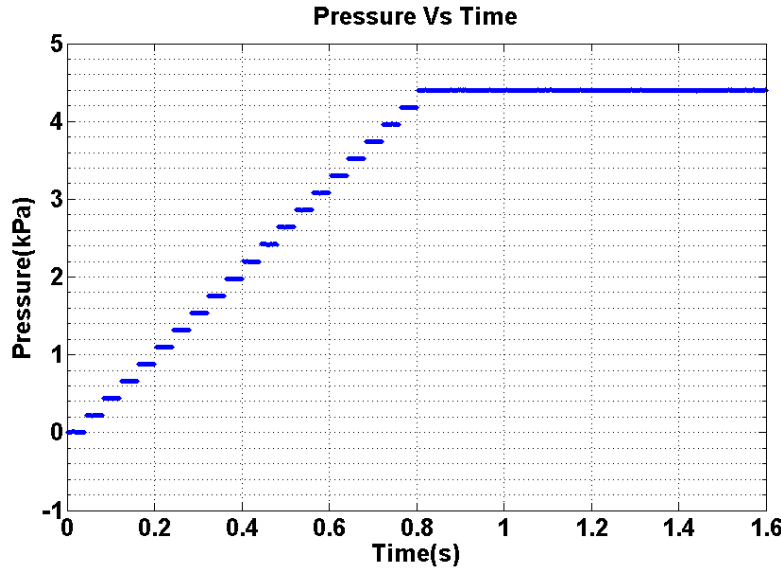
(b)

Figure 7. (a) DEM sphere packing immeresed into the LBM domain (b) Pressure variation **at the lower boundary of** the sample with time **for Test 1**.

tom boundaries as **defined** in Equation 15. However, changing parameters in this equation should be done with care in order to ensure incompressibility of the fluid. Carefully selecting the lattice space and time steps will ensure the minimum density variation across the lattice while saving computation time. In this study the LBM time step used was 1.212×10^{-4} s. **While the granular packing was bounded by vertical rigid walls, periodic boundary condition was applied on these boundaries for the LBM simulation.**

Snapshots of the particle configuration at different time intervals are shown in Figure 8. **At the begining of the simulation** (t=0.00 s), the particle bed is static and the velocities of the particles are zero. When the upward flow is uniformly introduced from the bottom, the resulting particle-fluid interaction force excites the particles. It can be observed that as the pressure gradient is gradually increased, dislodgement and mobilization of the particles begins due to the critical hydraulic gradient across the sample being reached. The particle fluid interaction force increases with the increase of pressure gradient, and movement of particles can be seen in the regions where the particle fluid interaction force is high enough to break the granular pack**ing**. At the initial stage, the top particles show higher
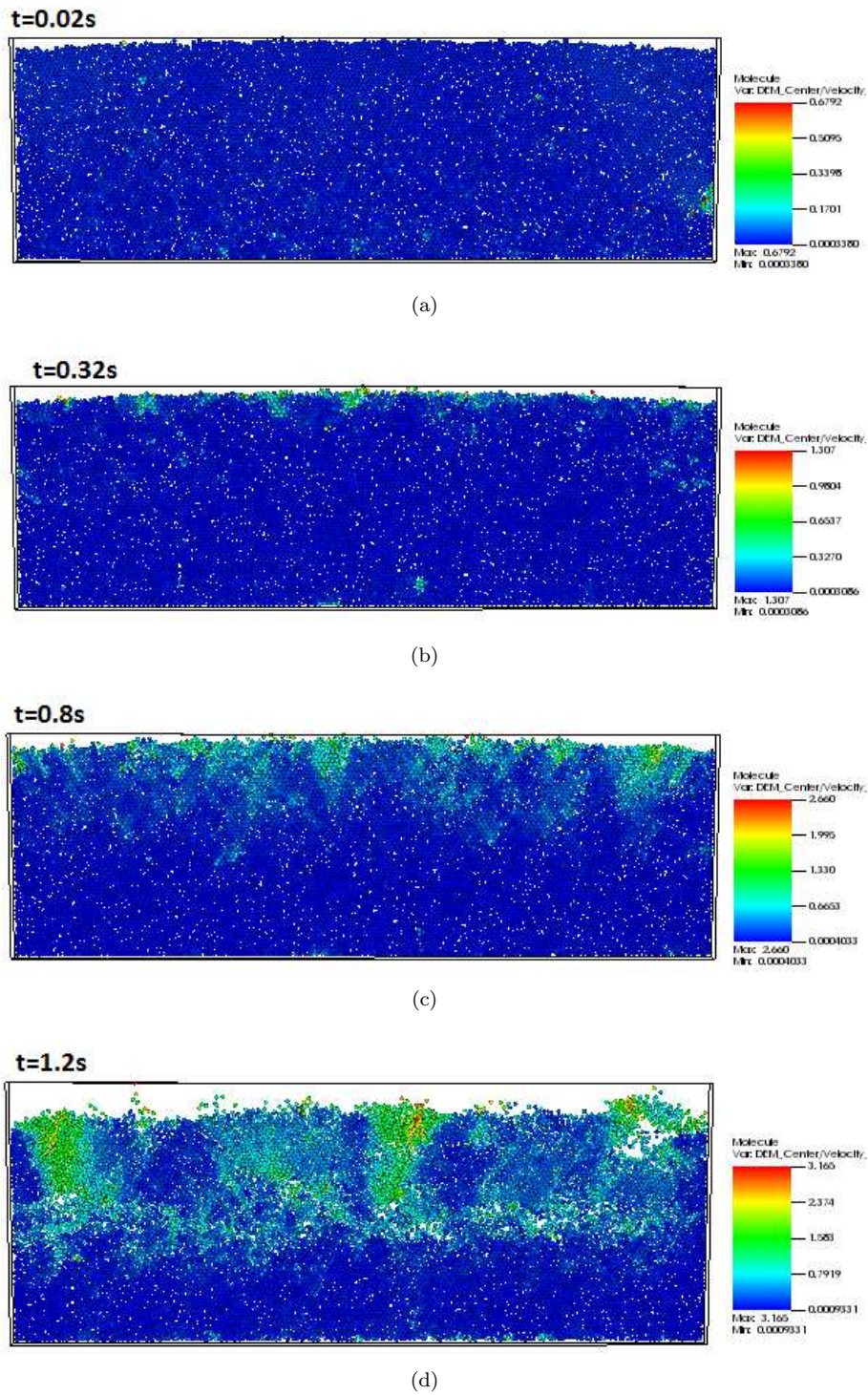
(a)

(b)

(c)

(d)

Figure 8.   Snapshots showing the flow patterns of the particles. Spheres are coloured according to their velocity (red for highest and blue for zero).

velocity than the others* and with time, detachment of particles starts from the top surface and propagates towards the bottom of the channel. As the material erodes, clear variation of porosity can be seen at the top of the sample.

Table 1.   Parameters used for the numerical simulation of upward pore fluid flow

| Parameters	Value
Container dimensions	300mm*6mm*140mm
Granular packing	**300mm*6mm*96mm**
Particle diameter	2mm
Number of particles	31473
Normal stiffness (Kn)	0.52kN/m
Tangential stiffness (Kt)	0.26kN/m
Friction coefficient	0.3
Particle density	$2500 \text{kg}/m^3$
Fluid density	$1000 \text{kg}/m^3$
Gravity	$\mathbf{10 m/s^2}$
Fluid viscosity	$1.6 \times 10^{-5} m^2/s$
Lattice spacing	**0.4mm**
LBM time step	1.212×10^{-4} s
Pressure applied	**4.4kPa**
Test 1: time to reach maximum pressure	**1.6s**
Test 2: time to reach maximum pressure	**0.8s**
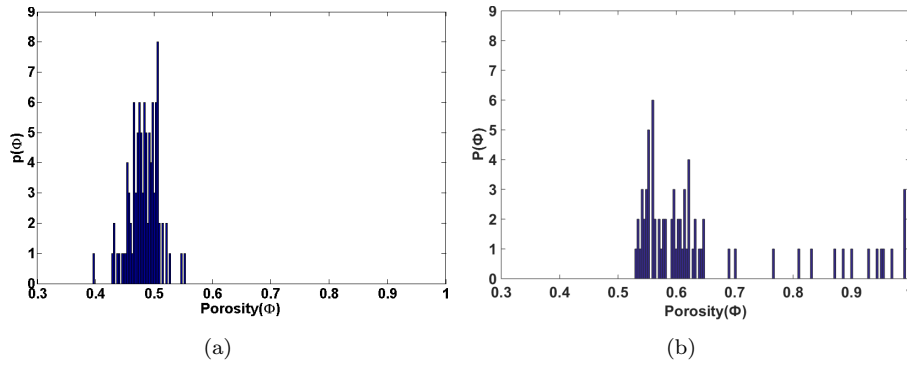
Figure 9.   Histrograms of the porosity variation of the porous pack: (a) before the start of the erosion process, and (b) after erosion is initiated.

4.   Model Verification

In order to verify the DEM/LBM model, porosity changes during the simulation were compared with experimental observations. Mahadevan et al. [33] have conducted similar physical experiments in a chamber with the aim of demonstrating erosion and channelization in a saturated porous medium. Experimental results showed that the porosity **variation of the sample** before the erosion started was **almost normally distributed with a mean porosity of approximately** 0.4. **After initiation of erosion, the overall porosity increased with increasing variation** leading to completely eroded channels represented by porosities equal to one. The simulation results showed similar porosity distributions but with **higher** porosity values compared to the experiment because mono-sphere packing was used (Figure 9). The agreement between simulated and measured porosity **distributions** is satisfactory.

5.   Simulation Results and Discussion

For identifying the onset of erosion, average values of the **parameters describing the state of the** fluid and solid phase were monitored during the simulation. Figure 10 shows the variation of pressure difference across the sample, linear momentum and porosity and co-ordination number changes with the height of the
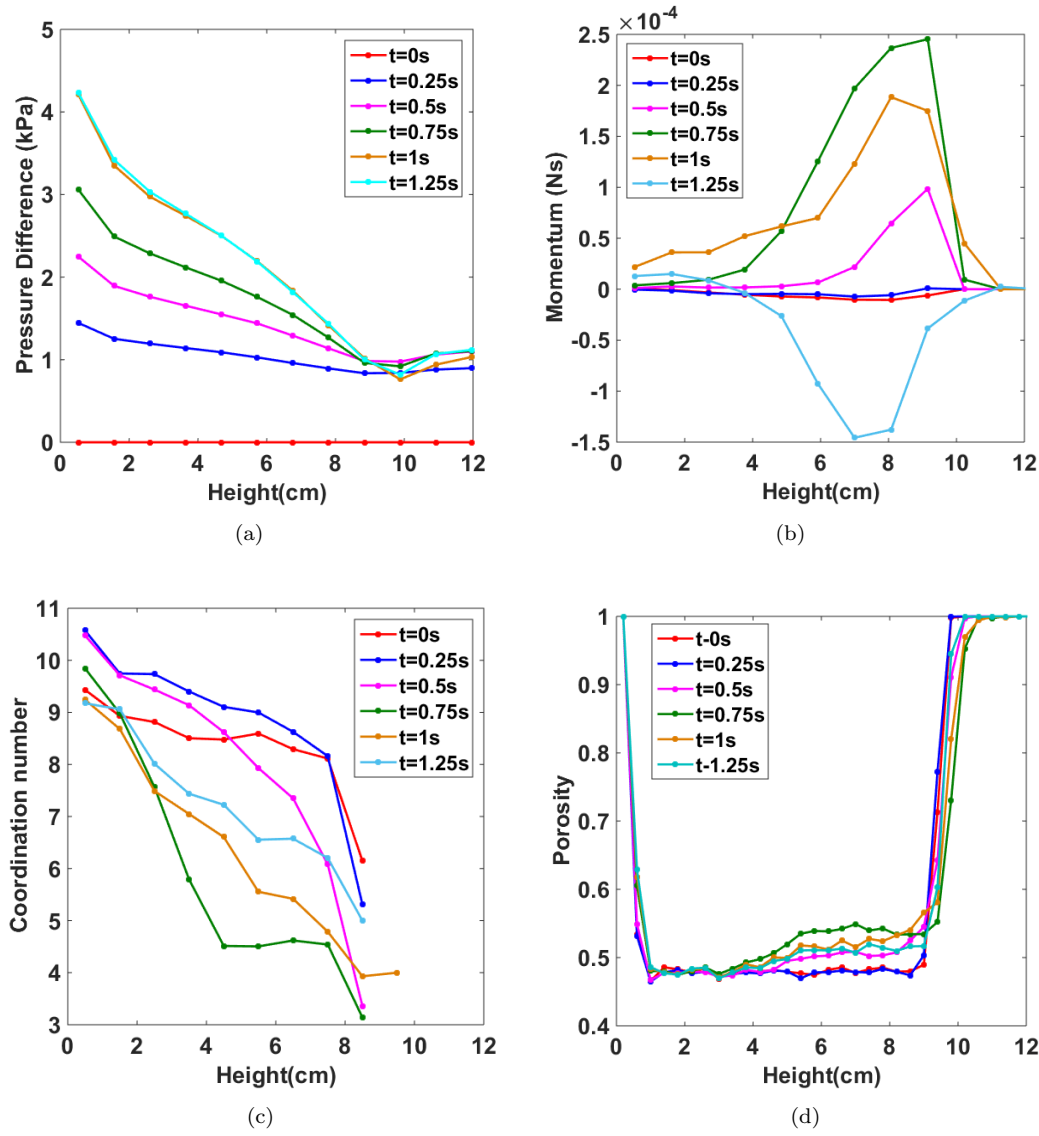
Figure 10. Fluid and particle properties variation with the height of the sample: (a) pressure difference vs height, (b) linear momentum vs height, (c) coordination number vs height, and (d) porosity vs height. **Note: the height of the DEM sample was initially 9.6 cm.**

sample at different time intervals **during the complete simulation time**.

Within 0.8 seconds the pressure at the lower boundary of the chamber had increased step-wise by 0.22 kPa increments to 4.4 kPa, which was then kept constant for the residual simulation time (Figure 7(b)). At the beginning of the simulation, the pressure distribution within the granular packing was almost linear. As the pressure gradient increased, the uppermost strata of the particles started to detach **(Figure 8) and the pressure distribution became increasingly non-linear (Figure 10(a)), increasing the bouyancy forces on the lower layers. Linear momentum increased with time in the upper part of the sample and propagated to the bottom of the chamber reaching its peak at around t = 0.75 s (Figure 10(b)).** This variation was well-matched with the **coordination number of the DEM packing (average number of contacts per particle), which reached a minimum when the linear momentum reached its maximum (Figure 10(c)). The** porosity profile across the sample showed **its highest value at around**
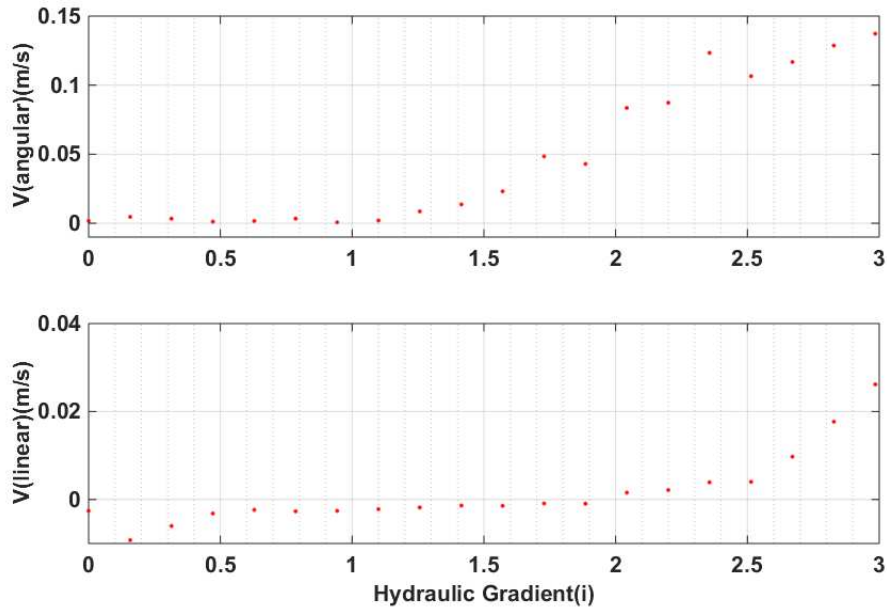
(a)
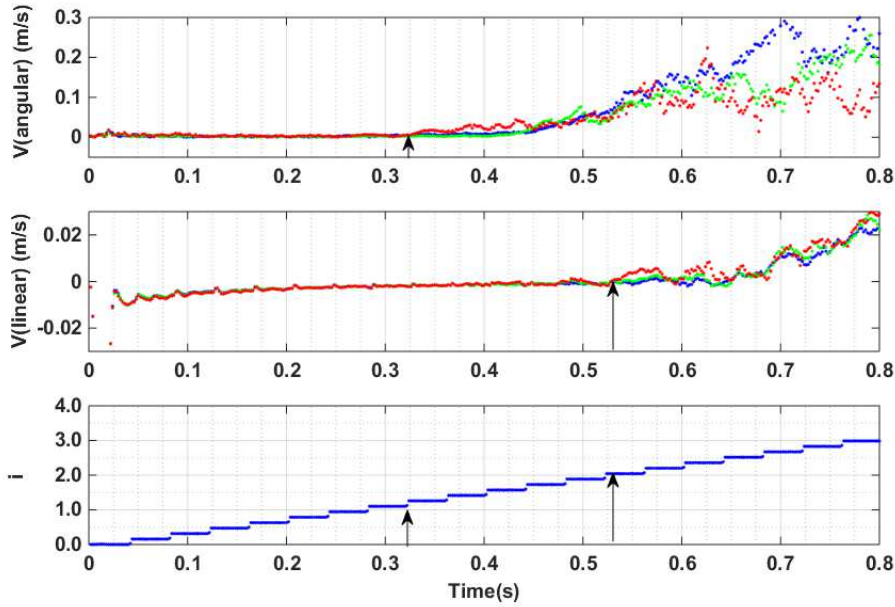
(b)

Figure 11. **Test 1:** (a) angular velocity (V(angular)) and linear velocity (V(linear)) of upper layer particles at last time step with hydraulic gradient across the sample; (b) linear velocity, angular velocity and hydraulic gradient (i) against time **for the first three layers of the sample (red: top-most layer, green: middle layer, blue: lowest layer, see Figure 6).**

t = 0.75 s which is well matched with other profiles. The height of the sample increased with time **reaching its maximum at t = 1 s. As can be seen in Figure 8, with ongoing simulation a zone of larger porosities has developed in the middle of the sample, which is also indicated by the low coordination number at t = 0.75 s. After t = 0.75 s, the coordination number increased and the linear momentum dropped to negative values accompanied by a reduction in the height of the samples indicating a collapse in that zone.**
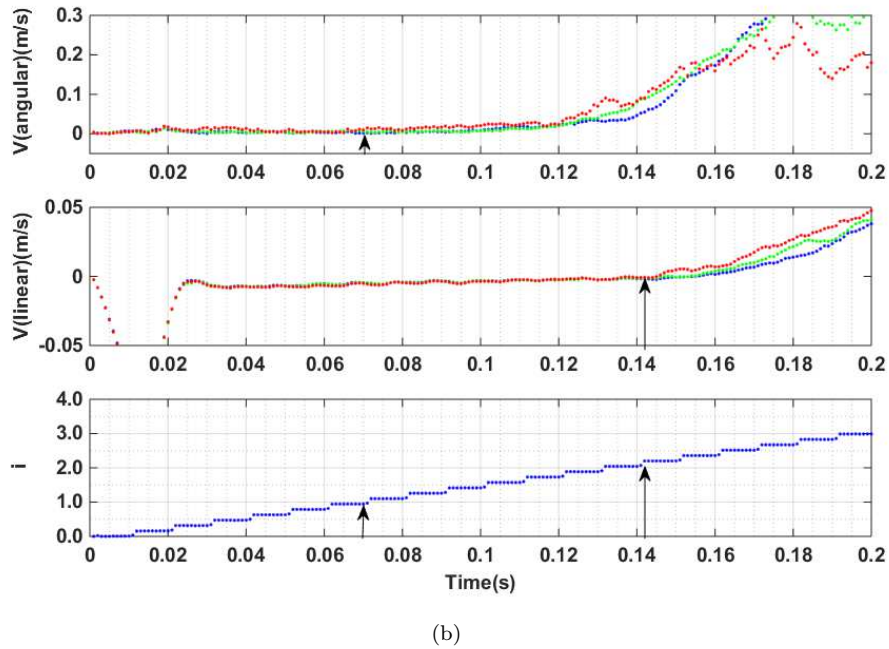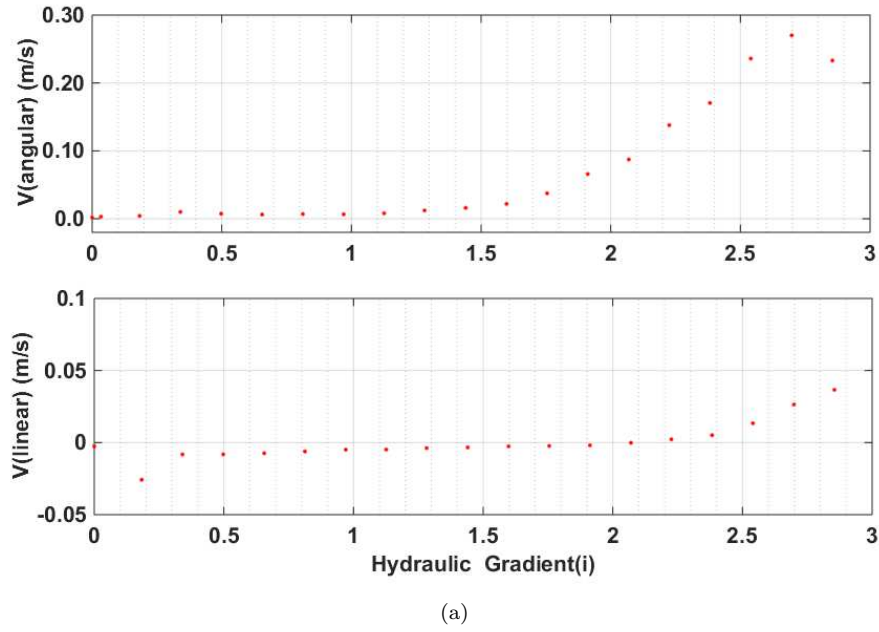
(a)

(b)

Figure 12.   **Test 2;** (a) angular velocity (V(angular)) and linear velocity (V(linear)) of upper layer particles at last time step against hydraulic gradient across the sample; (b) linear velocity, angular velocity and hydraulic gradient **against time for the first three layers of the sample (red: top-most layer, green: middle layer, blue: lowest layer, see Figure 6) with time.**

In order to identify the onset of erosion, micro-structural changes in the mechanical parameters of the particles forming at the upper boundary of the packing were analysed together with the overall gradient applied to the sample. Basically, there are two possible manifestations for the onset of erosion that are considered in this study: (i) movement of particles, and (ii) the loss of contact forces between particles both caused by the forces exerted by the flowing water. Two tests have been conducted for this study with two different times for reaching the

maximum pressure of 4.4 kPa (Table 1). Changes in angular and linear velocity for the uppermost particle layer independenty of the applied hydraulic gradient are shown for Test 1 in Figure 11(a) and for Test 2 in Figure 12(a). As the pressure gradient was applied step-wise over a limited time period, only the condition at the last time step of each pressure increment was considered for these plots. The evolution of both velocities during the simulation is shown for the first three particle layers (red, green and blue lines in Figure 6) together with the applied hydraulic gradient in Figure 11(b) for Test 1 and in Figure 12(b) for Test 2.

The results from Test 1 clearly show that angular movement of particles increases **at a lower hydraulic gradient of approximately 1** than the upward linear velocity with corresponding gradient of around 2. **Also in the temporal evolution of both velocities it becomes clear that** the rotational movement of particles is the first visible sign of the onset of erosion, which is shown by an increase of angular velocity at time t=0.32 s **corresponding to a gradient of 1.0.** Upward movement of the particles can be seen in the linear velocity **only at t=0.53 s** at a gradient of 2.0, which **confirms an** increase of upward translational velocity and formation of the loosened layer **visible in Figure 10.In line with Fleshman and John [34], this process of a granular bed becoming fluidised takes place** in four stages: (1) first visible movement, (2) heave progression, (3) boil formation, and (4) total heave. **The simulation results presented here cover the first two stages of this process.**

Test 2 was conducted to determine whether the onset of erosion is time dependent. **As can be seen in Figure 12(a),** the first small increase in angular velocity is seen at a hydraulic gradient i=1. While linear velocity increases at a hydraulic gradient i=2.2. **The temporal evolution of both velocities confirms this result. The angular velocity increases slightly at 0.07 s while the linear velocity shows an increase only after 0.14 s.** This result confirms that the onset of erosion is not time dependent for the presented model. **An important result of the presented simulations is the observation that angular movements take place earlier and at lower hydraulic gradients than linear movements of particles. This observation** can be considered as evidence of interlocking mechanisms acting between the particles, which are difficult **to observe experimentally and nearly impossible to be modelled** with frequently used continuous approaches. Due to the flow in pores towards particles sitting on top of the packing, inhomogeneous flow distributions occur on the surface of the uppermost particles leading to a **reduction of contact forces, and thus frictional shear stress, and as a consequence rotation caused by the** drag forces applied.

The analysis of the contact forces acting between particles reveal further information about the onset of erosion. As a vertical flow is introduced to the sample, the forces acting on the particles include; (1) gravitational force of the particle, (2) buoyancy force and seepage force; and (3) normal and tangential forces due to interaction between particles. The weight of the particle remains constant throughout the test. The initiation of the first **vertical** movement of particles occurs when the seepage force is equal to the addition of buoyant weight and inter-granular force. At this point the particles at the surface are in a state of equilibrium and start to move with increasing hydraulic gradient. Figure 13(a) shows, the variation of inter-particle forces with the height of the sample in Test 1. **At t=0 s water flow does not exist. With the onset of water flow the inter-particle force increases due to forces applied by the fluid and**
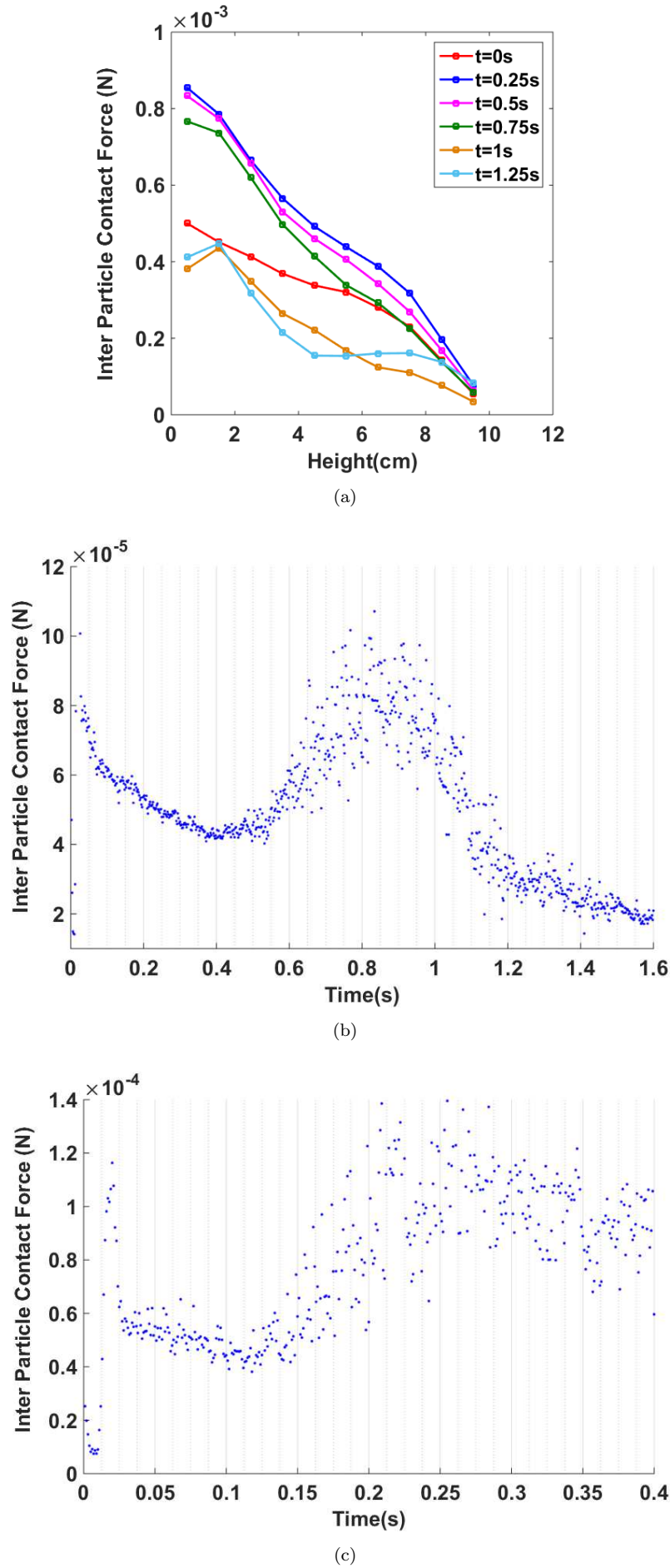
(a)

(b)

(c)

Figure 13. (a) Inter-particle contact force with height of the sample for Test 1, (b) Inter-particle contact force between particles in upper-most layer for Test 1, (c) Inter-particle contact force between particles in upper-most layer for Test 2.

the interlocking of particles. However, with time fluid forces start to lift particles in the upper part of the sample reducing the overburden pressure and thus the overall contact forces in the sample. Figure 13(b) and 13(c) show the variation of inter-particle force with time for the uppermost particle layer for Test 1 and Test 2, respectively. As can be seen, contact forces reduce to a minimum at about 0.4 s for Test 1 and at about 0.11 s for Test 2, which means the minimum contact force is reached a little later than the start of angular movement of the particles (t=0.32 s for Test 1 and 0.14 s for Test 2). This observation suggests that the angular movement of particles breaks the interaction between particles, which further reduces contact forces.

An important outcome of this micro-scale study is that the first visible manifestation of the onset of erosion is angular movements of particles in the upper layer of a granular packing. Although the existence of coarse particles sitting on top of a particle arrangement has been neglected in our model, this is a new finding, which will have a noteworthy impact on the interaction between finer and coarser particles during contact erosion. The rolling resistance has already been identified in a former numerical study as an important parameter influencing the mixing process between coarser and finer particles under the influence of water flow [15]. Another simplification made to save computation time in this study is the consideration of a rather thin chamber with rigid walls. Albeit interlocking effects of particles definitely exert an influence on the reaction of individual particles and the particle packing, some useful and very fundamental observations have been made during this study, such as the rotational movement of particles as the first manifestation for the onset of erosion as well as the development of preferential erosion channels in the fluidised bed as a self-organising effect of the process. Figure 8(d) shows clearly preferential particle movements by particle assemblies highlighted in green with a sharp transition to particles in rest, which are shown in blue. Though, this was not part of the presented study on the onset of erosion, this observation should be highlighted, since it was observed as well in a numerical study using a continuum model [36].

It will be a future task to further develop the numerical model to represent more realistic scenarios which include large particles and non-spherical particles. Furthermore, physical experiments are in preparation to investigate and quantify porosity changes during erosion on a micro- and macro-scale.

6.   Summary and Conclusions

This paper introduced a coupled DEM-LBM method for investigating the onset of erosion as a coupled hydrodynamic problem which occurs frequently in hydraulically loaded geotechnical structures. A simplified model was developed representing a mono dispersed packing of particles within a rectangular chamber **with rigid walls**. Seepage flow was applied from the lower end of the packing with a step-wise increase of the gradient across the sample. **The mechanical reaction of the** three **topmost particle** layers of the packing was analyzed to identify dislodging mechanisms. These mechanisms were considered as manifestations of instabilities characterizing the onset of erosion. The following observations were made in the numerical investigation:

(1) Particles started to rotate at an overall hydraulic gradient of 1.0. With increasing hydraulic gradient the angular movement increased until the first visible heave was observed. This observed angular movement was considered as evidence of interlocking mechanisms acting between the particles, which have been difficult to model with frequently used continuous approaches. Due to the water flow in pores towards particles sitting on top of the packing, inhomogeneous flow distributions occurred on the surface of the uppermost particles leading to rotation due to the drag forces applied. Future investigations aim to identify this observation in physical experiments.

(2) The movement of particles in a vertical direction took place at around a hydraulic gradient of 2.0, which was far higher than the hydraulic gradient commonly calculated, for example, using the relationship suggested by Terzaghi and Peck [35]. **The high value of the gradient as observed in the numerical model was caused probably by the chosen mechanic boundary conditions and the resulting interlocking effect of particles. This assumption will be a subject of future numerical investigations.**

(3) Although the size of the chamber, especially its thickness, was quite small, it was possible to replicate essential mechanisms of erosion, which also have been observed in the literature. So it was possible to show similar evolution of the changes in the statistical distributions of the porosity **as a result of the influence of flowing water** as they have been already observed in experiments [33]. Furthermore, another manifestation of erosion, which is the regular pattern of preferential movement of particles, could be observed in the experiments presented here. Similar results have been observed with a continuum-based model developed by Muhlhaus et al. [36].

(4) Inter-particle contact forces reduced to a minimum value shortly after the start of rotational movements of particles. This observation is proof of the effect that angular movement of particles causes further breakage of inter-particle forces in the pore structure further reducing the overall contact forces. An important question to be considered in future investigations is the influence of the particle shape on this effect.

Overall it can be summarised that the presented DEM-LBM method and the model chosen have proven to be effective for tracking micro-mechanical properties of fluid and particles **for investigating manifestations of the onset of erosion** with the available computational resources.

7. Acknowledgements

References

[1] J. Sherard, L. Dunnigan, J. Talbot, J. Geotech. Engrg, 110 (1984), p. 701.

[2] S. Bonelli, O. Brivois, R. Borghi, N. Benahmed, C. R. Mecanique, 334 (2006), p. 555.

[3] M. Foster, R. Fell, M. Spannagle, Can. Geotech. J., 37 (2000), p. 1000.

[4] R. Beguin, P. Philippe, Y.H. Faure, J. Hydraul. Eng., 139 (2013), p. 1.

[5] P.A. Cundall, O.D.L. Strack, Geotechnique, 29 (1979), p. 47.

[6] C.S. Chang, C.L. Liao, Int. J. of solids struct., 26 (1990), p. 437.

[7] C.S. Chang, L. Ma, Int. J. of solids struct., 28 (1991), p. 67.

[8] M. Oda, J. Konishi, S. Nemat-Nasser, Mech. of Mater., 1 (1982), p. 269.

[9] T.G. Sitharam, R. Sebestian, Proceedings of Indian Geotechnical Conference, Kochi, 284 (2011).

[10] E. Onate, M.A. Celigueta, S.R. Idelsohn, Acta Geotechnica, 1 (2006) p.237.

[11] U. EI Shamy, A coupled continuum fluid-discrete particle hydro-mechanical model for granular soil liquefaction, PhD thesis, Rensselaer Polytechnic Institute, Troy, NY (2004).

[12] U. EI Shamy, F. Aydin, J. Geotech. Geoenviron., 134 (2008), p. 1385.

[13] U. EI Shamy, M. Zegal, J. Eng. Mech., 131 (2005), p. 413.

[14] N. Xiao-dong, W. Yuan, International forum on porous flow and applications, China, (2009)

[15] S. Galindo-Torres, A. Scheuermann, H. Muhlhaus and D.J.Williams, Acta Geotechnica (2013) p. 1.

[16] J.J. Derksen, Phys. Fluids, 113303 (2011) p. 1.

[17] F.Lomine, L. Scholts, L. Sibille, P. Poullain, Int. J. Numer. Meth. Engng., 37 (2011) p. 577.

[18] Y. Abdelhamid, U. EI Shamy, Int. J. Numer. Anal. Meth. Geomech., 38 (2014) p. 142.

[19] E.I.S. Usama., M. Zegal , J. Eng. Mech., 131 (2005), p. 413.

[20] J.P. Plassiard, F.V.Donz, Structural Engineering International 19 (2009): p. 333.

[21] K. Han, Y.T. Feng, D.R.J. Owen, Int. J. Numer. Meth. Engng., 66 (2006) p. 485.

[22] S.A. Galindo-Torres, Comput. Methods Appl. Mech. Engrg., 265 (2013), p. 107.

[23] S. Luding, Granular Matter, 10 (2008) p. 235.

[24] S.A. Galindo-Torres, D.M. Pedroso, D.J. Williams, L. Li, Comput. Phys. Commun., 183 (2012) p. 266.

[25] J. Hardy, O.D. Pazzis, Y. Pomeau, Phys. Rev. 13 (1976) p. 1949.

[26] Y. Han, P.A. Cundall, Int. J. Numer. Meth. Fluids, 67 (2011) p. 314.

[27] Y. Qian , D. d'Humieres, P. Lallemand, EPL¿(Euophys. Lett.) 17 (1992) p. 479.

[28] X. Le, L. Luo, J. Stat. Phys. 88 (1997) p. 927.

[29] D.R.J. Owen, C.R. Leonardi, Y.T. Feng, Int. J. Numer. Meth. Engng. 87 (2010) p. 66.

[30] D.R. Noble, J.R. Torczynski, Int. J. of Mod. Phys. C09 (1998) p. 1189.

[31] F. White, *Viscous Fluid Flow*, McGraw-Hill New York, 1991.

[32] M. Sukop, D. Thorne, *Lattice Boltzmann modelling: an introduction for geoscientists and engineers*, Springer Verlag,Heidelberg, 2006.

[33] A. Mahadevan, A.V. Orpe, A. Kudrolli, L. Mahadevan, EPL. 98 (2012) p. 58003.

[34] M.S. Fleshman, D.R John, Int. J. Geotech. Geoenviron. Eng. 140 (2014) p. 04014017-1.

[35] K. Terzaghi, R.B. Peck, *Soil Mechanics in engineering practice*, Wiley, New York, 1948.

[36] H. Muhlhaus, L. Gross, A. Scheuermann, Acta Geotechnica, 10 (2014) p.333.